

The peculiar abundances of HE 1005–1439^{***}

A carbon-enhanced extremely metal-poor star contaminated with products of both *s*- and *i*-process nucleosynthesis

Partha Pratim Goswami^{1,2} and Aruna Goswami¹

¹ Indian Institute of Astrophysics, Koramangala, Bangalore 560034, India
e-mail: partha.pg@iiap.res.in; aruna@iiap.res.in

² Pondicherry University, R.V. Nagar, Kalapet, 605014, Puducherry, India

Received 12 July 2021; Accepted 08 September 2021

ABSTRACT

Context. Understanding the surface chemical composition of carbon-enhanced metal-poor (CEMP) stars with enhanced abundances of heavy elements remains problematic.

Aims. One of the primary objectives is to investigate the origin of the peculiar abundance pattern observed in the carbon-enhanced extremely metal-poor (EMP) object HE 1005–1439, which is enriched with both *s*-process and *i*-process nucleosynthesis products and thus forms a new class of object with a distinct abundance pattern.

Methods. We performed a detailed, high-resolution spectroscopic analysis of this object based on SUBARU/HDS spectra with a resolution R of $\sim 50\,000$. We utilised the line analysis method with measured equivalent widths of neutral and ionised lines due to various elements. Moreover, we calculated the spectrum synthesis of carbon molecular bands and lines due to elements with hyperfine structures to determine the elemental abundances. Abundances of ten light elements from C through Ni and 12 heavy elements Sr, Y, Ba, La, Ce, Pr, Nd, Eu, Dy, Er, Hf, and Pb were determined. We also performed a parametric-model-based analysis of the abundances of the heavy elements to understand the origin of the observed abundance pattern.

Results. For the first time, we came across an object with a surface chemical composition that exhibits contributions from both slow (*s*) and intermediate (*i*) neutron-capture nucleosynthesis. The observed abundance pattern is quite unique and has never been observed in any CEMP stars. The star is found to be a CEMP-s star based on the CEMP stars' classification criteria. However, the observed abundance pattern could not be explained based on theoretical *s*-process model predictions. On the contrary, our parametric-model based analysis clearly indicates its surface chemical composition being influenced by similar contributions from both the *s*- and *i*-process. We critically examined the observed abundances and carefully investigated the formation scenarios involving *s*-process and *i*-process that are available in literature, and we found that none of them could explain the observed abundances. We note that the variation we see in our radial velocity estimates obtained from several epochs may indicate the presence of a binary companion. Considering a binary system, we therefore propose a formation scenario for this object involving effective proton ingestion episodes (PIEs) triggering *i*-process nucleosynthesis followed by *s*-process asymptotic giant branch (AGB) nucleosynthesis with a few third-dredge-up (TDU) episodes in the now extinct companion AGB star. Results obtained from the parametric-model-based analysis are discussed in light of existing stellar evolutionary models.

Key words. Stars: Individual [HE 1005–1439]; Stars: Abundances; Stars: Carbon; Stars: Chemically peculiar

1. Introduction

Carbon-enhanced metal-poor (CEMP) stars form an important class of metal-poor giants, sub-giants, and dwarfs, with a large fraction of them showing enhanced abundances of heavy elements (see Beers & Christlieb (2005) and Frebel (2018) for a general review). Among the different types of CEMP stars, the CEMP-s stars are enriched with products of *s*-process nucleosynthesis, the CEMP-r stars are enriched with the products of *r*-process

nucleosynthesis, and CEMP-r/s stars are enriched with products of *i*-process nucleosynthesis. Understanding the diverse abundance patterns exhibited by different groups of CEMP stars that are believed to be associated with different formation mechanisms has been a challenge. In Goswami et al. (2021), we present a detailed analysis and discussion on the classification criteria of CEMP stars, as well as the formation scenarios of CEMP stars put forward by different authors (Cowan & Rose 1977; Hill et al. 2000; Qian & Wasserburg 2003; Cohen et al. 2003; Jonsell et al. 2006; Campbell & Lattanzio 2008; Campbell et al. 2010; Stancliffe et al. 2011; Herwig et al. 2011; Doherty et al. 2015; Abate et al. 2016; Jones et al. 2016; Banerjee et al. 2018; Clarkson et al. 2018; Denissenkov et al. 2017; Côté et al. 2018). In this paper, we report an extremely

* Based [in part] on data collected at the Subaru Telescope, which is operated by the National Astronomical Observatory of Japan (NAOJ).

** Part of the data are retrieved from the JVO portal (<http://jvo.nao.ac.jp/portal>) operated by the NAOJ.

metal-poor carbon-enhanced star, HE 1005–1439, whose surface chemical composition is found to be enriched with both *s*-process and *i*-process nucleosynthesis that forms a new class of object with a distinct abundance pattern. The peculiar abundance pattern, observed for the first time in a CEMP star, was investigated based on a parametric-model-based analysis that revealed almost equal contributions from both the *s*-process and the *i*-process to its surface chemical composition. We examined various production mechanisms and formation scenarios for this object. A formation scenario involving effective proton ingestion episodes (PIEs) triggering *i*-process nucleosynthesis followed by *s*-process asymptotic giant branch (AGB) nucleosynthesis with limited third-dredge-up (TDU) episodes seems to be most promising for this type of object.

Literature surveys show that this object had been studied earlier by different groups (Aoki et al. 2007; Schuler et al. 2008; Yong et al. 2013; Caffau et al. 2017). However, these studies were limited by the number of elements for which abundances were estimated. As the abundances of the neutron-capture elements except Ba are not reported in the literature, we re-visited the object and estimated the atmospheric parameters as well as abundances of ten light elements and twelve heavy elements. The derived abundances were then carefully investigated with an aim to understand the origin and formation mechanism(s) of the object.

2. Source of spectra

The wavelength-calibrated high-resolution ($R \sim 50\,000$) spectra of HE 1005–1439 used in this study are retrieved from the SUBARU archive¹. Spectra obtained at four different epochs using the high-dispersion spectrograph (HDS) (Noguchi et al. 2002) attached to the 8.2m Subaru Telescope cover the 3515–6780 Å wavelength range. The spectra acquired on October 26, 2002 (single exposure), and December 8, 2003 (five exposures) cover 4020–6780 Å with a gap of ~ 70 Å from 5370–5440 Å, and the spectra acquired on October 28, 2002 (single exposure) and May 26, 2003 (three exposures) cover the 3515–5270 Å wavelength region with a gap of 15 Å from 4380–4395 Å. For our studies, spectra obtained on the same dates are combined to increase the signal-to-noise ratio (S/N). The sample spectra of the programme star at two different wavelength regions are shown in Figure 1.

3. Radial velocities and stellar atmospheric parameters

We measured the radial velocity of HE 1005–1439 from spectra acquired at four different epochs using several clean unblended lines. The estimated radial velocities with 98.54 ± 0.75 km s⁻¹ (October 26, 2002), 99.17 ± 0.90 km s⁻¹ (October 28, 2002), 48.95 ± 0.46 km s⁻¹ (May 26, 2003), and 103.53 ± 0.46 km s⁻¹ (December 8, 2003) show that the object is a radial velocity variable, and that it is likely to be in a binary system.

We determined the photometric temperatures of HE 1005–1439 using broad-band colours with colour-

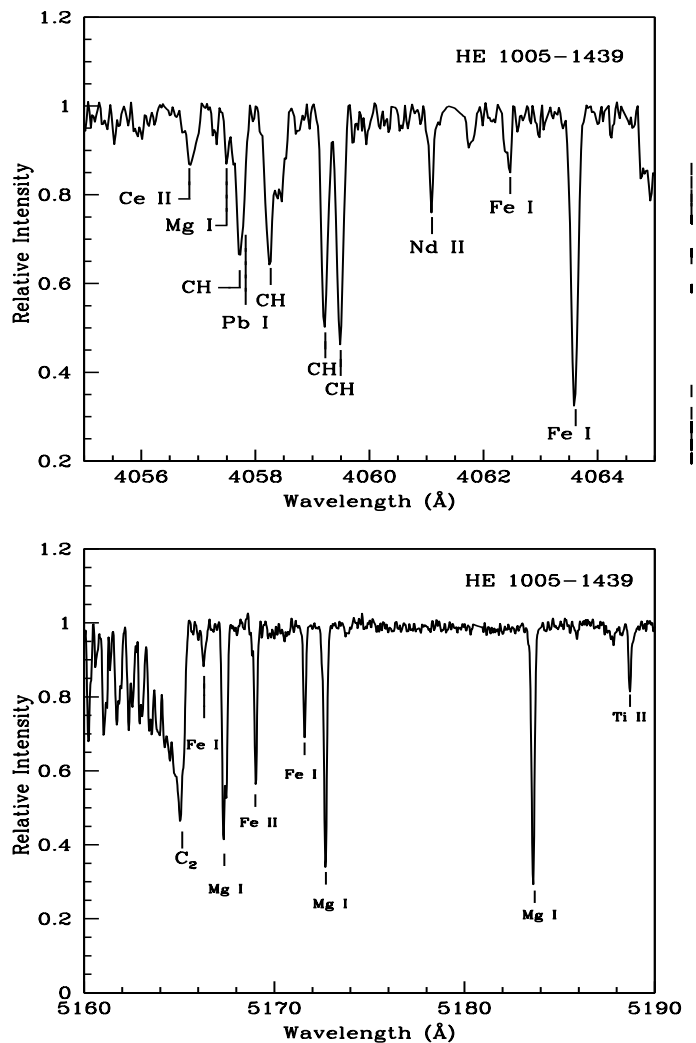


Fig. 1. Sample spectra of the programme star in the 4055–4065 Å (upper panel) and 5160–5190 Å (bottom panel) wavelength regions.

temperature calibrations available for giants (Alonso et al. 1999) based on the infrared flux method (IRFM) following the procedure described in Goswami et al. (2006, 2016). The 2MASS photometric magnitudes for J, H, and K are taken from Cutri et al. (2003). The photometric temperatures corresponding to (B–V), (V–K), (J–H), and (J–K) at $[\text{Fe}/\text{H}] \sim -3.0$ are found to be $T_{\text{eff}}(\text{B–V}) = 4650$ K, $T_{\text{eff}}(\text{V–K}) = 5323$ K, $T_{\text{eff}}(\text{J–H}) = 4817$ K, and $T_{\text{eff}}(\text{J–K}) = 5017$ K, respectively. As the photometric temperature $T_{\text{eff}}(\text{J–K})$ is independent of metallicity (Alonso et al. 1996, 1999), we used $T_{\text{eff}}(\text{J–K})$ as an initial guess for estimating the spectroscopic temperature of HE 1005–1439 through an iterative process of selecting the appropriate model atmosphere.

Following the detailed procedure described in Goswami et al. (2021), the stellar atmospheric parameters T_{eff} , $\log g$, micro-turbulent velocity (ζ), and metallicity $[\text{Fe}/\text{H}]$ of the programme star are derived using 45 clean lines of Fe I and five lines of Fe II. The excitation potentials of these lines are in the 0.0–5.0 eV range. The list of lines

¹ <http://jvo.nao.ac.jp/portal>

with the measured equivalent widths and atomic line information is presented in Table A.1.

An updated version of MOOG software by Sneden (Sneden 1973) that assumes local thermodynamic equilibrium (LTE) conditions was used for our analysis. The model atmospheres are used from the Kurucz grid of model atmospheres with no convective overshooting². The solar abundances are adopted from (Asplund et al. 2009). The effective temperature and the micro-turbulent velocity are fixed by the conventional methods of excitation potential balance and equivalent width balance. The ionisation equilibrium method of equating the abundance of Fe derived from neutral and ionised Fe lines determines the surface gravity. The metallicity is given by the abundance of Fe derived from Fe I and Fe II lines. The estimates of stellar parameters along with the literature values are listed in Table 1.

Our estimate of effective temperature is 170 K higher than that of Aoki et al. (2007). Aoki et al. (2007) estimated the effective temperature from (V–K), (V–R), (V–I), and (R–I) photometric colour indices, using the empirical temperature calibration scale of Alonso et al. (1999). In general, due to the presence of C₂ and CN molecular bands in carbon enhanced stars, (V–K) gives lower temperature than the other colour indices. However, in the case of HE 1005–1439 temperature estimate from T_{eff}–(V–K) calibration relation is found to be much higher than those obtained from other colour indices. This was also noticed by Aoki et al. (2007) and due to this discrepancy, adopted a lower value for temperature (~ 5000 K) closer to those derived using different colour indices. Yong et al. (2013) estimated the effective temperature of HE 1005–1439 using IRFM adopting the colour-temperature relations given in Ramírez & Meléndez (2005). Our estimate of effective temperature is close to that of Yong et al. (2013).

Our estimate of micro-turbulent velocity (ζ) is lower than that of Aoki et al. (2007) and Yong et al. (2013). For their analysis, Yong et al. (2013) used the same measured equivalent widths and lines reported by Aoki et al. (2007). While Aoki et al. (2007) used 19 lines of Fe I covering a range of equivalent widths 16.7 mÅ – 88.0 Å, we have used 45 lines of Fe I covering a range of equivalent widths 15.6 Å – 127.1 Å. With more clean lines covering a good range in line strength, we are confident about our estimated micro-turbulent velocity.

Our measured surface gravity $\log g$ is similar to that of Aoki et al. (2007). The $\log g$ derived by Aoki et al. (2007) is based on the ionisation equilibrium method similar to the one that we have used. Yong et al. (2013) used Y² isochrones (Demarque et al. 2004) to determine $\log g$, assuming an age of 10 Gyr, and $[\alpha/\text{Fe}] = +0.3$ and reported a higher $\log g$ (~ 2.55) for this object.

We estimated the mass of HE 1005–1439 from its position in the Hertzsprung-Russell (HR) diagram ($\log(L/L_{\odot})$ versus $\log(T_{\text{eff}})$ plot). The value of the parallax (= 0.2733 mas) is taken from Gaia Collaboration et al. (2018) and the V (= 13.52) magnitude is taken from SIMBAD. The bolometric correction is determined based on the empirical calibration equations of Alonso et al. (1999). Interstellar extinction for HE 1005–1439 is calculated using the formulae by Chen et al. (1998). The value of $\log(L/L_{\odot})$ is found to be ~ 1.83. We have used the updated BaSTI-IAC evolu-

tionary tracks³ (Hidalgo et al. 2018) generated for $[\text{Fe}/\text{H}] = -3.2$ and $[\alpha/\text{Fe}] = 0.4$, including overshooting and diffusion, to estimate the mass of the star. The mass of the object is found to be 0.8 M_⊙. The $\log g$ value is calculated using the following relation:

$$\log(g/g_{\odot}) = \log(M/M_{\odot}) + 4\log(T_{\text{eff}}/T_{\text{eff}\odot}) + 0.4(M_{\text{bol}} - M_{\text{bol}\odot}). \quad (1)$$

The adopted solar values are $\log g_{\odot} = 4.44$, $T_{\text{eff}\odot} = 5770$ K and $M_{\text{bol}\odot} = 4.74$ mag (Yang et al. 2016). Using this method, we found a $\log g$ (~ 2.32) comparable to that of Yong et al. (2013). This value is much larger than our spectroscopic $\log g$ value ~1.8. We note that the evolutionary tracks and isochrones highly depend on the opacity in the stellar atmosphere. As BaSTI-IAC evolutionary tracks are generated using normal carbon and without considering the influence of high carbon, $\log g$ values determined using such evolutionary tracks and isochrones may lead to erroneous estimates. This may also explain the discrepancy between the $\log g$ values obtained by us from spectroscopy and that reported by Yong et al. (2013). We used the spectroscopic $\log g$ value for our analysis.

4. Results & discussions

4.1. Abundance analysis

We determined the elemental abundances by measuring the equivalent widths of the absorption lines due to neutral and ionised species of several elements and/or by applying a spectrum synthesis technique using the radiative transfer code MOOG (Sneden 1973) that assumes LTE and model atmospheres from the Kurucz grid of model atmospheres with no convective overshooting⁴. Elemental abundances of C, Na, Mg, Ca, Sc, Ti, Cr, and Mn, iron-peak elements Co and Ni, and neutron-capture elements Sr, Y, Ba, La, Ce, Pr, Nd, Eu, Dy, Er, Hf, and Pb were estimated. We used the method of spectrum synthesis calculations for elements showing hyperfine splitting (e.g. Sc, Mn, Ba, La, and Eu). The lines used in the analysis with the measured equivalent widths and atomic line information are presented in Table A.1. Atomic line information, such as the excitation potential and $\log gf$ values, were taken from the Kurucz database of atomic line list. The abundance results along with the literature values are presented in Table 2.

4.1.1. Light elements

We used spectrum synthesis calculations for estimating the abundances of carbon from molecular bands of carbon. The abundance of carbon was derived using the CH band near 4310 Å and C₂ bands near 5160 Å and 5635 Å (Figure 2). The slight difference in A(C) derived from C₂ and CH molecular bands might have appeared due to the difference in S/N in the regions of the CH and C₂ bands. The S/N of the spectra near 5200 Å (i.e. near the C₂ bands) is ~ 130, while the S/N is ~ 50 near 4320 Å (i.e. near the CH band). Carbon is found to be enhanced in HE 1005–1439 with $[\text{C}/\text{Fe}] \sim 2.37$. The estimated carbon isotopic ratio

³ <http://basti-iac.oa-abruzzo.inaf.it/>

⁴ <http://kurucz.harvard.edu/grids.html>

² <http://kurucz.harvard.edu/grids.html>

Table 1. Derived atmospheric parameters of our programme star, and literature values.

Star name	T_{eff} (K)	$\log g$ (cgs)	ζ (km s^{-1})	[Fe I/H]	[Fe II/H]	[Fe/H]	Ref
HE 1005–1439	5170	1.80	1.26	-3.04 ± 0.15	-3.01 ± 0.03	-3.03	1
	5000	1.90	2.00	-3.17 ± 0.32	-3.15 ± 0.22	-3.17	2
	5202	2.55	1.60	-	-	-3.09	3
	5030	-	-	-	-	-	4

References: 1. Our work; 2. Aoki et al. (2007); 3. Yong et al. (2013); 4. Gaia Collaboration et al. (2018).

$^{12}\text{C}/^{13}\text{C}$, obtained from spectrum synthesis calculations of the C_2 band near 4740 Å (Figure 3) is ~ 5.0 . We have taken the line lists of C_2 bands at 5165 Å, 5635 Å, and 4740 Å, and of the CH band at 4310 Å from the ‘linemake’⁵ atomic and molecular line database.

While HE 1005–1439 is enhanced in Na ($[\text{Na}/\text{Fe}] = 1.37$), Mg ($[\text{Mg}/\text{Fe}] = 0.53$) is moderately enhanced. Gehren et al. (2004) found that the systematic NLTE corrections required on the abundances of Na and Mg in case of metal-poor halo stars are -0.4 and $+0.1$, respectively.

The other light elements, Ca, Sc, Ti, Co, and Ni, are moderately enhanced in HE 1005–1439. The abundances of Cr and Mn are found to be sub-solar. However, Bergemann & Gehren (2008) and Bergemann et al. (2010) have found that in case of metal-poor giants, abundances of Co and Mn are underestimated in LTE calculations. Bergemann & Gehren (2008) performed NLTE calculations for Mn on a sample of fourteen stars and found that the NLTE abundances of Mn in all the sample stars are higher than the LTE abundances, in fact, the NLTE correction may go up to $0.5 - 0.7$ dex at low metallicities. NLTE calculations done by Bergemann et al. (2010) for Co I lines revealed that the corrections may vary from $0.1 - 0.8$ dex depending on the effective temperature and metallicity. They found that deviation from LTE is larger in the case of giants than it is for dwarfs. Our estimates of the abundances of light elements are found to match closely with the literature values (calculated with LTE assumption) of the programme star within error bars. Hyperfine splitting contributions of the lines (Table A.1) used for spectrum synthesis calculations of Sc and Mn are taken from linemake.

4.1.2. Neutron-capture elements

While HE 1005–1439 is found to be enhanced ($[\text{X}/\text{Fe}] > 1.0$) in heavy elements Ba, La, Ce, Pr, Nd, Er, Hf, and Pb, the elements Sr, Y, Eu, and Dy are moderately enhanced ($[\text{X}/\text{Fe}]$ in the range 0.26 to 0.72). We could not detect lines due to Tc. Hyperfine splitting contributions for the spectrum synthesis calculations of the lines Ba II 5853.67 Å & Ba II 6141.71 Å are taken from McWilliam (1998) and for La II 4921.78 Å line the hyperfine splitting contributions are taken from Jonsell et al. (2006). For the spectrum synthesis calculations of the lines Ba II 6496.90 Å, La II 4086.71 Å,

⁵ *linemake* contains laboratory atomic data (transition probabilities, hyperfine and isotopic substructures) published by the Wisconsin Atomic Physics and the Old Dominion Molecular Physics groups. These lists and accompanying line list assembly software have been developed by C. Sneden and are curated by V. Placco at <https://github.com/vmplacco/linemake>.

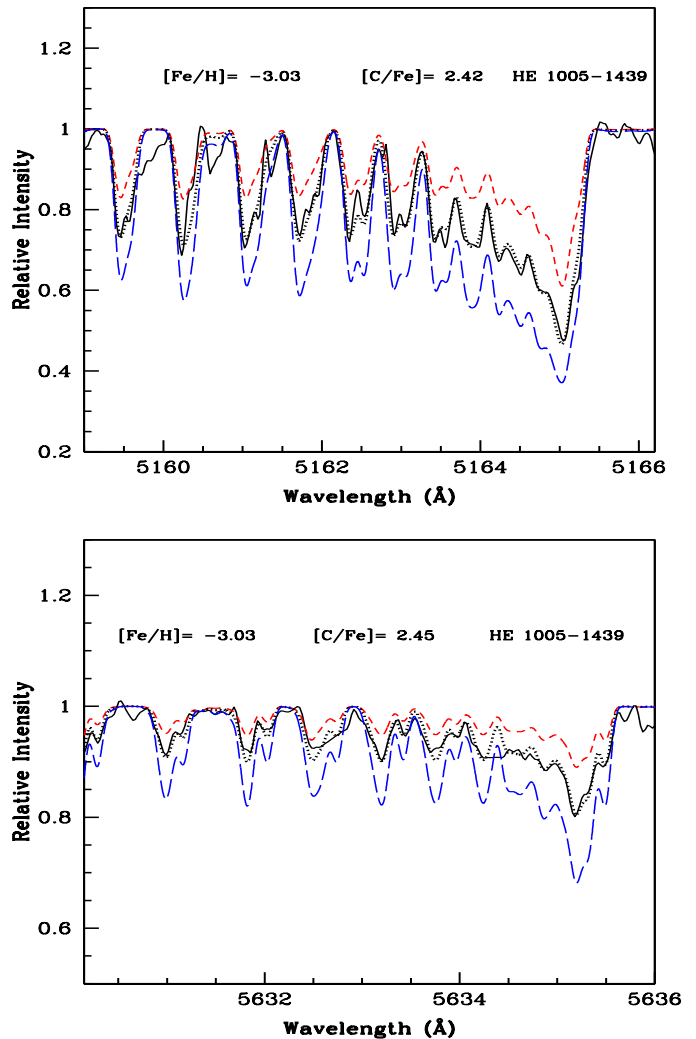


Fig. 2. Spectral synthesis fits of C_2 bands around 5165 Å (top panel) and 5635 Å (bottom panel). The dotted lines indicate the synthesised spectra and the solid lines indicate the observed spectra. Two alternative synthetic spectra are shown corresponding to $\Delta[\text{C}/\text{Fe}] = +0.3$ (long-dashed line) and $\Delta[\text{C}/\text{Fe}] = -0.3$ (short-dashed line).

La II 4123.22 Å, Eu II 4129.73 Å, and Eu II 4205.04 Å, the hyperfine splitting contributions are taken from linemake. The abundance of Pb is estimated using the spectrum synthesis calculation of Pb I 4057.81 Å.

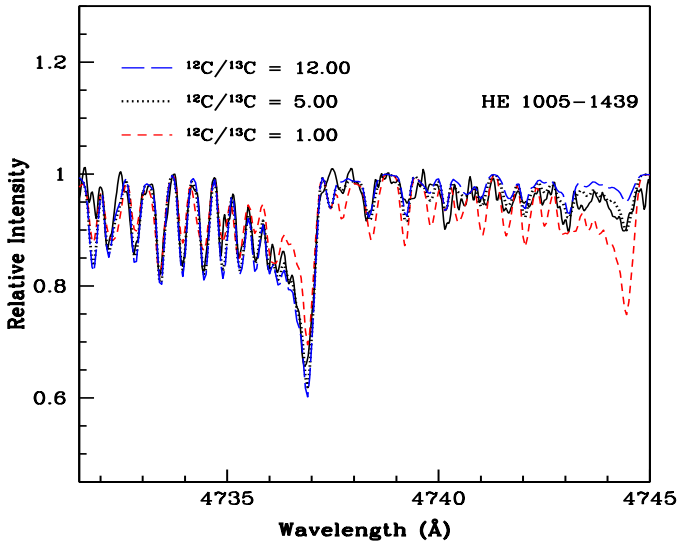


Fig. 3. Spectral synthesis fits (dotted curves) of the C_2 features around 4740 Å obtained with the adopted C abundance and $^{12}C/^{13}C$ value (dotted curve). The observed spectrum is shown by a solid curve. Two alternative fits with $^{12}C/^{13}C \sim 1$ (short-dashed line) and 12 (long-dashed line) are shown to illustrate the sensitivity of the line strengths to the isotopic carbon abundance ratios.

4.2. Abundance uncertainties

We estimated the total uncertainties on the elemental abundances as discussed in Goswami et al. (2021). Two components, namely random error ($\sigma_{ran} = \frac{\sigma_s}{\sqrt{N}}$, where σ_s represents the standard deviation of the abundance of a particular species derived using N number of lines of that species) and systematic error (σ_{sys}), contribute to the total uncertainties. While the random error arises due to the uncertainties on the factors like oscillator strength, equivalent width measurement, and line blending, the systematic error arises due to the uncertainties in estimating the stellar atmospheric parameters. Finally, the uncertainties on $[X/Fe]$ are derived as follows:

$$\sigma_{[X/Fe]}^2 = \sigma_{\log\epsilon}^2 + \sigma_{[Fe/H]}^2, \quad (2)$$

$$\sigma_{\log\epsilon}^2 = \sigma_{ran}^2 + \sigma_{sys}^2, \quad (3)$$

$$\begin{aligned} \sigma_{sys}^2 = & \left(\frac{\delta \log\epsilon}{\delta T} \right)^2 \sigma_{T_{eff}}^2 + \left(\frac{\delta \log\epsilon}{\delta \log g} \right)^2 \sigma_{\log g}^2 \\ & + \left(\frac{\delta \log\epsilon}{\delta \zeta} \right)^2 \sigma_{\zeta}^2 + \left(\frac{\delta \log\epsilon}{\delta [Fe/H]} \right)^2 \sigma_{[Fe/H]}^2, \end{aligned} \quad (4)$$

where, $\sigma_{T_{eff}} = 100$ K, $\sigma_{\log g} = 0.2$ dex, $\sigma_{\zeta} = 0.2$ km/s⁻¹, and $\sigma_{[Fe/H]} = 0.15$ dex represent the typical uncertainties on the stellar atmospheric parameters T_{eff} , $\log g$, ζ , and $[Fe/H]$, respectively. We evaluated the partial derivatives appearing in Equation 4 for the programme star, varying the stellar parameters T_{eff} , $\log g$, ζ , and $[Fe/H]$ by ± 100

K, ± 0.2 dex, ± 0.2 km/s⁻¹, and ± 0.2 dex, respectively. We note that the uncorrelated nature of the uncertainties arising from the different stellar parameters in Equation 4 may lead to the overestimation of the calculated uncertainties on $\log \epsilon$ and $[X/Fe]$. The estimated uncertainties $\sigma_{\log\epsilon}$ and $\sigma_{[X/Fe]}$ are listed in columns 5 and 8, respectively, of Table 2.

4.3. Interpretation of results

Our analysis shows the object HE 1005–1439 to be an extremely metal-poor star with $[Fe/H] = -3.03$ in accordance with Aoki et al. (2007). Carbon and neutron-capture elements are found to be enhanced in the programme star. Following the classification criteria of CEMP stars (Goswami et al. 2021), the object is found to belong to the CEMP-s sub-group (Figure 4a). However, as shown in Figure 4b, the ratio of heavy-s process (hs) elements (Ba, La, Ce, and Nd) to the light-s process (ls) elements (Sr and Y), $[hs/ls]$ (~ 0.92) is closer to the value at which the CEMP-r/s stars peak (1.06) (Goswami et al. 2021).

Using the s -process yields calculated using the FRUITY⁶ model (Straniero et al. 2006; Cristallo et al. 2009b, 2011, 2015) at the same metallicity ($z=0.00002$) of the programme star, and considering different masses, we were not able to reproduce the observed abundance pattern of heavy elements. In Figure 5a, we show a comparison of the observed elemental abundances with the AGB model yields (normalised to the La abundance of HE 1005–1439), calculated for $M = 1.3 M_{\odot}$ and $M = 2.0 M_{\odot}$. As can be seen in the top panel of the residual plot of Figure 5d, the s -process AGB models over-produce the light s -process elements Sr and Y, under-produce the elements Pr, Er, and Hf, and over-produce the third s -process peak element Pb.

In Figure 5b, we show a comparison of the i -process model yields of Hampel et al. (2016) (normalised to the La abundance of HE 1005–1439), calculated for $n = 10^{12}$ cm⁻³ and $n = 10^{14}$ cm⁻³, with the observed elemental abundance pattern of the programme star. The i -process models (Hampel et al. 2016) alone at neutron-densities $n = 10^{12} - 10^{15}$ cm⁻³ cannot satisfactorily reproduce the observed abundance pattern of the programme star either. We can see from the middle panel of residual plot (Figure 5d) that the i -process model with $n = 10^{12}$ cm⁻³ fits the light s -process elements Sr and Y satisfactorily but under-produces Ce and Pr. Again, i -process model with $n = 10^{14}$ cm⁻³ under-produces the light s -process elements Sr and Y but over-produces Ba, Eu, and Er. The diverse abundance pattern observed in HE 1005–1439, which could not be explained either by s -process AGB nucleosynthesis or by the i -process alone, prompted us to explore alternate production mechanisms that might have influenced its surface chemical composition.

4.3.1. Parametric-model-based study

We performed a parametric-model-based study to delineate the contributions of s -, i - and r -processes to the observed abundances of heavy elements of the programme star. We used s -process model yields of the FRUITY model at different masses ($M = 1.3$ – $2.0 M_{\odot}$), the Solar System r -process residual pattern (stellar model) given in Arlandini et al.

⁶ <http://fruity.oa-teramo.inaf.it/>

Table 2. Elemental abundances in HE 1005–1439

	Z	solar $\log\epsilon^{(a)}$	$\log\epsilon$ (dex)	$\sigma_{\log\epsilon}$	[X/H]	[X/Fe]	$\sigma_{[X/Fe]}$	[X/Fe] (^b)	[X/Fe] (^c)	[X/Fe] (^d)
C (CH, 4310 Å)	6	8.43	7.65 (syn)	0.23	-0.78	2.25	0.27	2.48	-	2.14**
C (C ₂ , 5165 Å)	6	8.43	7.82 (syn)	0.22	-0.61	2.42	0.27	-	-	-
C (C ₂ , 5635 Å)	6	8.43	7.85 (syn)	0.21	-0.58	2.45	0.26	-	-	-
Na I	11	6.24	4.58±0.03 (2)	0.16	-1.66	1.37	0.22	1.19	1.05	-
Mg I	12	7.60	5.10±0.05 (4)	0.12	-2.50	0.53	0.19	0.60	0.33	-
Ca I	20	6.34	3.78±0.18 (10)	0.10	-2.56	0.47	0.18	0.57	0.54	-
Sc II	21	3.15	0.82±0.10 (2)	0.17	-2.33	0.70	0.23	-	-	-
Sc II*	21	3.15	0.75±0.00 (2)	0.15	-2.40	0.63	0.23	-	-	-
Ti I	22	4.95	2.27±0.17 (4)	0.14	-2.68	0.35	0.21	0.48	0.49	-
Ti II	22	4.95	2.23±0.20 (8)	0.12	-2.72	0.31	0.20	0.19	0.31	-
Cr I	24	5.64	2.59±0.15 (5)	0.17	-3.05	-0.02	0.23	-0.38	-0.34	-
Mn I	25	5.43	2.56±0.14 (2)	0.25	-2.87	0.16	0.29	-	-	-
Mn I*	25	5.43	2.13±0.03 (2)	0.23	-3.30	-0.27	0.28	-	-	-
Fe I	26	7.50	4.46±0.15 (45)	0.15	-3.04	-	-	-	-	-
Fe II	26	7.50	4.49±0.03 (5)	0.10	-3.01	-	-	-	-	-
Co I	27	4.99	2.20±0.07 (3)	0.13	-2.79	0.24	0.20	-	-	-
Ni I	28	6.22	3.40 (1)	0.23	-2.82	0.21	0.28	-	-	-
Sr II	38	2.87	0.10±0.22 (2)	0.27	-2.77	0.26	0.31	-	-	-
Y II	39	2.21	-0.40±0.27 (3)	0.18	-2.61	0.42	0.23	-	-	-
Ba II	56	2.18	0.64±0.27 (3)	0.28	-1.54	1.49	0.31	-	-	-
Ba II*	56	2.18	0.31±0.24 (3)	0.27	-1.87	1.16	0.31	1.06	1.17	-
La II	57	1.10	-0.61±0.12 (3)	0.13	-1.71	1.32	0.20	-	-	-
La II*	57	1.10	-0.68±0.06 (3)	0.11	-1.78	1.25	0.19	-	-	-
Ce II	58	1.58	-0.07±0.17 (3)	0.14	-1.65	1.38	0.21	-	-	-
Pr II	59	0.72	-0.76 (1)	0.22	-1.48	1.55	0.27	-	-	-
Nd II	60	1.42	-0.36±0.15 (4)	0.13	-1.78	1.25	0.20	-	-	-
Eu II*	63	0.52	-2.05±0.18 (2)	0.17	-2.57	0.46	0.22	-	-	-
Dy II	66	1.10	-1.21±0.19 (3)	0.15	-2.31	0.72	0.21	-	-	-
Er II	68	0.92	-1.05±0.20 (2)	0.17	-1.97	1.06	0.23	-	-	-
Hf II	72	0.85	-0.73±0.01 (2)	0.16	-1.58	1.45	0.18	-	-	-
Pb II*	82	1.75	0.70 (1)	0.11	-1.05	1.98	0.19	-	-	-

$$^{12}\text{C}/^{13}\text{C} (\text{C}_2, 4740 \text{ \AA}) = 5.0$$

* abundance is derived using spectrum synthesis calculations. ** abundance is derived using [C I] line. The number inside the parenthesis shows the number of lines used for the abundance determination.

References: (^a) Asplund et al. (2009); (^b) Aoki et al. (2007); (^c) Yong et al. (2013); (^d) Schuler et al. (2008).

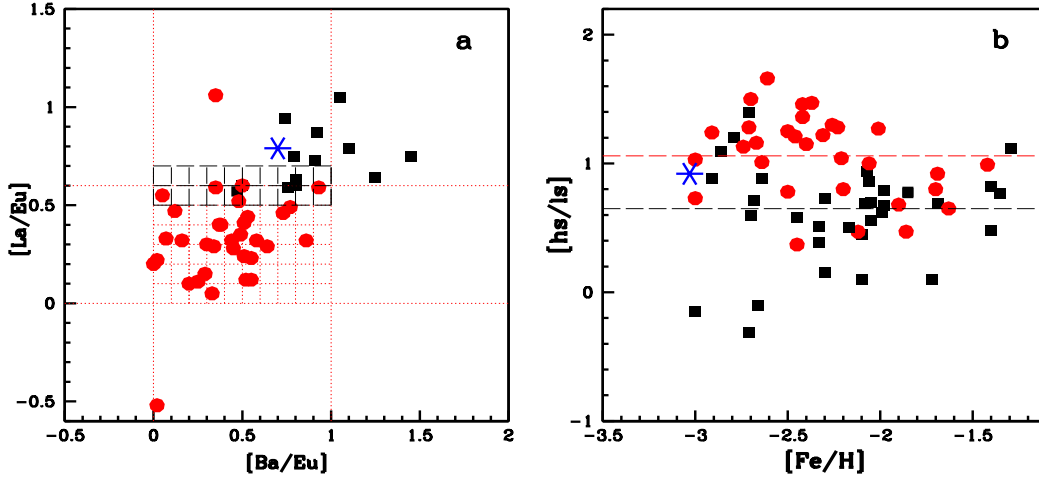


Fig. 4. Filled red circles and filled black squares respectively represent literature CEMP-r/s and CEMP-s stars compiled by Goswami et al. (2021), and the blue star represents the programme star. *panel a:* Grid formed by the dotted red lines bound by $0.0 < [\text{La}/\text{Eu}] < 0.6$ and $0.0 < [\text{Ba}/\text{Eu}] < 1.0$ indicates the region defined for CEMP-r/s stars by Goswami et al. (2021). The grid formed by the black dashed lines bound by $0.5 < [\text{La}/\text{Eu}] < 0.7$ represents the region where $[\text{Eu}/\text{Fe}] > 1.0$ classifies the stars as CEMP-r/s and $[\text{Eu}/\text{Fe}] < 1.0$ classifies the stars as CEMP-s. *panel b:* Red dashed line at $[\text{hs}/\text{ls}] = 1.06$ and the black dashed line at $[\text{hs}/\text{ls}] = 0.65$ represent the peaks of $[\text{hs}/\text{ls}]$ for CEMP-r/s and CEMP-s, respectively, as shown by Goswami et al. (2021) in Figure 13(a).

(1999), and *i*-process model yields of Hampel et al. (2016) at different neutron-densities ($n = 10^{12}$ – 10^{15} cm $^{-3}$). We excluded the element Pb from the parametric-model based study as the *i*-process model yields of Pb are not reported by Hampel et al. (2016). We normalised the elemental abundances of the models to the La abundance of HE 1005–1439. The observed elemental abundances of HE 1005–1439 are then fitted with the parametric-model function $\log \epsilon_j = C_s N_{sj} + C_i N_{ij} + C_r N_{rj}$, where N_{sj} , N_{ij} , and N_{rj} indicate the normalised abundance from the *s*-process, *i*-process, and *r*-process, respectively. Here, C_s , C_i , and C_r indicate the component coefficients corresponding to contributions from the *s*-process, *i*-process, and *r*-process, respectively. In order to find the best fit, we calculated χ^2 for all the possible combinations of models of *s*-process ($M = 1.3$ – $2.0 M_\odot$) and *i*-process ($n = 10^{12}$ – 10^{15} cm $^{-3}$) along with solar *r*-process residues. The minimum χ^2 is achieved for a combination of an *s*-process model with $M = 2.0 M_\odot$ and an *i*-process model with $n = 10^{14}$ cm $^{-3}$ with no contribution from the *r*-process. The parametric-model function gives an excellent fit to the light *s*-process elements Sr and Y and a satisfactory fit to the heavier neutron-capture elements. The best parametric-model fit, where the contribution from both *s*- and *i*-process are similar ($C_s = 0.56$, $C_i = 0.44$), is shown in Figure 5c and the bottom panel of the residual plot (Figure 5d).

4.3.2. Origin of the programme star: Possible formation scenarios

The parametric-model-based study clearly established that the surface chemical composition of HE 1005–1439 is influenced by almost equal contributions of *s*-process AGB nucleosynthesis and *i*-process nucleosynthesis. We attempted to capture a formation scenario for this object involving a binary picture. Our assumption on binarity is profoundly based on the radial velocity variations observed on a few epochs. The low value of $^{12}\text{C}/^{13}\text{C}$ (~ 5.0) measured for HE 1005–1439 also points towards the extrinsic nature of carbon, and hence the heavy elements in the star. In the intrinsic carbon stars (as they are in AGB phase), third-dredge-up (TDU) episodes bring ^{12}C and *s*-process material to the surface, and the $^{12}\text{C}/^{13}\text{C}$ ratio can increase up to > 100 depending on the initial mass of the object (Karakas & Lattanzio 2014). However, in extrinsic carbon giants, such as HE 1005–1439, the $^{12}\text{C}/^{13}\text{C}$ ratio decreases due to the first dredge-up (FDU), which brings ^{13}C produced in the internal CNO cycle to the stellar atmosphere (Smith et al. 1993). Attributing the *s*-process contribution to the AGB mass-transfer scenario in the binary system, we carefully examined if any of the proposed formation scenarios of *i*-process nucleosynthesis available in literature could explain the *i*-process contribution in the observed abundance pattern of HE 1005–1439.

We investigated if the very late thermal pulse (VLTP) scenario proposed to explain the peculiar abundance pattern of the Sakurai object (V4334 Sagittarii) by Herwig et al. (2011) could explain the abundance peculiarities of HE 1005–1439. However, a characteristic property of VLTP in pre-white dwarf of producing light *s*-process elements 2 dex more than that of heavy *s*-process elements is not observed in HE 1005–1439.

Low-metallicity or zero-metallicity massive (20–30 M_\odot) stars (Banerjee et al. 2018) and super-AGB stars (9–11

M_\odot) (Jones et al. 2016) can pollute the ISM with *i*-process yields. However, an AGB mass-transfer scenario in a binary system formed from the *i*-process-enriched ISM also cannot explain the peculiar abundance pattern of the programme star due to its inadequacy to describe the low observed Pb abundance in HE 1005–1439. As shown in Figure 5a and the top panel of Figure 5d, the observed Pb abundance of HE 1005–1439 is about 0.30–0.60 dex lower than the prediction of the FRUITY model (Cristallo et al. 2009b, 2016) at $[\text{Fe}/\text{H}] \sim -3.0$. Pb is the main product of the *s*-process in AGB stars at low metallicities (Cristallo et al. 2009b). The low Pb abundance of HE 1005–1439 is difficult to explain by the scenario of pre-enrichment of ISM with *i*-process material or a scenario involving any external source of *i*-process material such as rapidly accreting white dwarfs (Denissenkov et al. 2019). This is because in these cases Pb would be more than (if the *i*-process neutron exposure (τ) of the progenitor is sufficient to produce enough Pb) or at a similar level to the *s*-process prediction, but it would not be less, as Pb is not destroyed in β -decay.

We propose that the surface chemical composition of HE 1005–1439 may be attributed to mass-transfer from a now extinct AGB companion with both *s*- and *i*-process nucleosynthesis occurring under suitable conditions during its evolution at different thermal pulses. Such a formation scenario may not be unlikely as many studies on the evolution of AGB stars have shown that neutron densities required for *s*-process and *i*-process can be achieved in the intershell region with the help of the partial mixing of protons in the radiative conditions (Herwig 2000; Denissenkov & Tout 2003; Herwig et al. 2003; Cristallo et al. 2009b, 2011; Piersanti et al. 2013; Karakas & Lattanzio 2014) and efficient PIEs in the convective conditions (Hollowell et al. 1990; Fujimoto et al. 2000; Iwamoto et al. 2004; Campbell & Lattanzio 2008; Lau et al. 2009; Cristallo et al. 2009a, 2016; Choplin et al. 2021), respectively.

In a certain study (Cristallo et al. 2009a) on the AGB evolution of a 1.5 M_\odot model with $[\text{Fe}/\text{H}] = -2.45$ without α enhancement, it was found that a strong PIE is followed by a deep TDU. Due to the PIE, H-burning occurring in high-temperature convective conditions creates a huge amount of ^{13}C , which leads to an efficient neutron production with neutron densities of the order of 10^{15} cm $^{-3}$. The study also noted that the convective He-shell splits into two subshells when the energy released by proton capture reactions slightly exceeds the energy production at the base of the convective shell. In the lower sub-shell, the $^{13}\text{C}(\alpha, n)^{16}\text{O}$ reaction produces *i*-process neutron density, and the nucleosynthesis path goes away from the valley of β stability producing a very high local $[\text{hs}/\text{ls}]$ ratio. The upper sub-shell, where the CNO cycle is the main energy source, later gets engulfed by the envelope. After that, a standard TP-AGB phase follows with repetitive TPs and TDUs, and *s*-process nucleosynthesis occurs. The number of expected stars experiencing PIEs is significantly reduced with the introduction of α -element enhancements (Cristallo et al. 2016).

Cristallo et al. (2009a) noted that the minimum mass of the models to experience TDU is significantly lowered by PIEs. Their model, after the PIE, encounters 25 additional TDU episodes, each of which is followed by radiative burning of the ^{13}C pocket. Although the final abundance pattern is a combination of *i*- and *s*-processes, excessive *s*-process

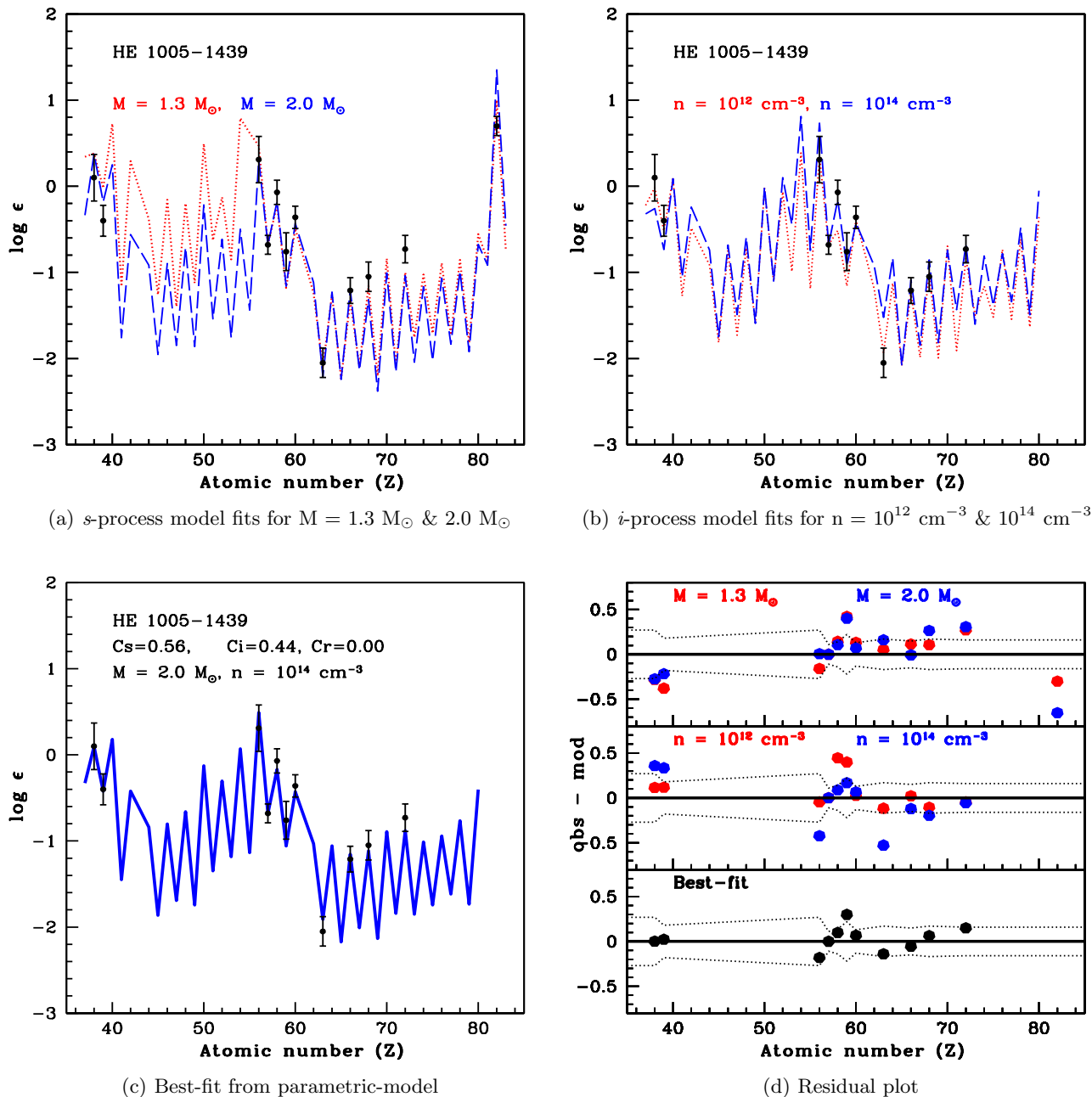


Fig. 5. Examples of theoretical model fits with the observed abundances of the star. In panels (a), (b), and (c), the points with error bars indicate the observed abundances.

nucleosynthesis after the PIE would remove the trace of the *i*-process and thus reduce the $[\text{hs}/\text{ls}]$ ratio.

In a recent study on the evolution of a $1 M_{\odot}$ object at low metallicity ($[\text{Fe}/\text{H}] = -2.5$), Choplin et al. (2021) noticed three convective instabilities occurring at the beginning of the TP-AGB phase. The main PIE occurs during the third instability, which produces high neutron densities of about $4.3 \times 10^{14} \text{ cm}^{-3}$ and rich *i*-process nucleosynthesis occurs. We note that although they are of similar metallicities, while in the model of Choplin et al. (2021) no further TPs were possible after the main PIE, in that of Cristallo et al. (2009a) 25 TPs after the PIE masked the

contribution of the *i*-process and resulted in an *s*-process surface abundance pattern.

We propose that a model that undergoes PIEs during the beginning of the TP-AGB phase (producing an *i*-process abundance pattern) followed by limited TPs (producing an *s*-process abundance pattern) might explain the abundance peculiarity of HE 1005-1439. This scenario is also likely to explain the low-Pb abundance in the programme star. The abundance of Pb depends on the time-integrated neutron-exposure (τ). From Figure 1 of Hampel et al. (2019), it is clear that as neutron density increases, production of Pb starts at higher τ . Therefore, a low Pb abundance may indicate that due to the operation of both *i*- and *s*-processes

in succession, neither of the processes received sufficient exposure time to produce enough Pb expected at $[\text{Fe}/\text{H}] \sim -3.0$.

5. Conclusions

A detailed, high-resolution spectroscopic study of the EMP star HE 1005–1439 revealed a peculiar abundance pattern different from those typically exhibited by CEMP stars. While the CEMP stars' classification criteria place the object in the CEMP-s group, the value of $[\text{hs}/\text{ls}] \sim 0.9$ is closer to the value (1.06) at which CEMP-r/s stars peak. The abundance pattern could not be reproduced either by the *s*-process or the *i*-process model predictions alone. However, a parametric-model based analysis clearly indicated that similar contributions from both the *s*- and *i*-process might have resulted in the observed abundance pattern of HE 1005–1439. We propose that the origin of the observed peculiar abundance pattern may be attributed to mass transfer from a now extinct AGB companion where both *i*- and *s*-process nucleosynthesis took place during various stages of the AGB evolution with PIEs triggering *i*-process followed by *s*-process AGB nucleosynthesis with a few TDU episodes.

Several uncertainties such as initial mass, metallicity, treatment of opacities, nuclear rates, and mixing mechanisms affect the theoretical understanding of AGB stars. The observational constraints derived from the programme star and the proposed scenario might provide a link for a better understanding of the interplay between PIEs and partial mixing of protons in the intershell region and also the conditions resulting in a pure *s*- or *i*-process surface abundance pattern in low-mass, low-metallicity AGB stars. We believe that the proposed scenario will be helpful in explaining the overlap of $[\text{hs}/\text{ls}]$ ratio in CEMP-s and CEMP-r/s stars (see Fig 13 of Goswami et al. (2021)) and the smooth transition of elemental abundances from the CEMP-s to CEMP-r/s regime (Goswami et al. 2021).

Acknowledgements. Funding from DST SERB project EMR/2016/005283 is gratefully acknowledged. We thank Melanie Hampel for the *i*-process yields. We thank the referee Elisabetta Caffau for many constructive suggestions and useful comments. This work made use of the SIMBAD astronomical database, operated at CDS, Strasbourg, France, the NASA ADS, USA and data from the European Space Agency (ESA) mission Gaia (<https://www.cosmos.esa.int/gaia>), processed by the Gaia Data Processing and Analysis Consortium (DPAC), <https://www.cosmos.esa.int/web/gaia/dpac/consortium>).

References

Abate, C., Stancliffe, R. J., & Liu, Z.-W. 2016, *A&A*, 587, A50
 Alonso, A., Arribas, S., & Martínez-Roger, C. 1996, *A&A*, 313, 873
 Alonso, A., Arribas, S., & Martínez-Roger, C. 1999, *A&AS*, 140, 261
 Aoki, W., Beers, T. C., Christlieb, N., et al. 2007, *ApJ*, 655, 492
 Arlandini, C., Käppeler, F., Wisshak, K., et al. 1999, *ApJ*, 525, 886
 Asplund, M., Grevesse, N., Sauval, A. J., & Scott, P. 2009, *ARA&A*, 47, 481
 Banerjee, P., Qian, Y.-Z., & Heger, A. 2018, *ApJ*, 865, 120
 Beers, T. C. & Christlieb, N. 2005, *ARA&A*, 43, 531
 Bergemann, M. & Gehren, T. 2008, *A&A*, 492, 823
 Bergemann, M., Pickering, J. C., & Gehren, T. 2010, *MNRAS*, 401, 1334
 Caffau, E., Bonifacio, P., Starkenburg, E., et al. 2017, *Astronomische Nachrichten*, 338, 686
 Campbell, S. W. & Lattanzio, J. C. 2008, *A&A*, 490, 769

Campbell, S. W., Lugaro, M., & Karakas, A. I. 2010, *A&A*, 522, L6
 Chen, B., Vergely, J. L., Valette, B., & Carraro, G. 1998, *A&A*, 336, 137
 Choplin, A., Siess, L., & Goriely, S. 2021, *A&A*, 648, A119
 Clarkson, O., Herwig, F., & Pignatari, M. 2018, *MNRAS*, 474, L37
 Cohen, J. G., Christlieb, N., Qian, Y.-Z., & Wasserburg, G. J. 2003, *ApJ*, 588, 1082
 Côté, B., Denissenkov, P., Herwig, F., et al. 2018, *ApJ*, 854, 105
 Cowan, J. J. & Rose, W. K. 1977, *ApJ*, 212, 149
 Cristallo, S., Karinkuzhi, D., Goswami, A., Piersanti, L., & Gobrecht, D. 2016, *ApJ*, 833, 181
 Cristallo, S., Piersanti, L., Straniero, O., et al. 2011, *ApJS*, 197, 17
 Cristallo, S., Piersanti, L., Straniero, O., et al. 2009a, *PASA*, 26, 139
 Cristallo, S., Straniero, O., Gallino, R., et al. 2009b, *ApJ*, 696, 797
 Cristallo, S., Straniero, O., Piersanti, L., & Gobrecht, D. 2015, *ApJS*, 219, 40
 Cutri, R. M., Skrutskie, M. F., van Dyk, S., et al. 2003, *VizieR Online Data Catalog*, II/246
 Demarque, P., Woo, J.-H., Kim, Y.-C., & Yi, S. K. 2004, *ApJS*, 155, 667
 Denissenkov, P. A., Herwig, F., Battino, U., et al. 2017, *ApJ*, 834, L10
 Denissenkov, P. A., Herwig, F., Woodward, P., et al. 2019, *MNRAS*, 488, 4258
 Denissenkov, P. A. & Tout, C. A. 2003, *MNRAS*, 340, 722
 Doherty, C. L., Gil-Pons, P., Siess, L., Lattanzio, J. C., & Lau, H. H. B. 2015, *MNRAS*, 446, 2599
 Frebel, A. 2018, *Annual Review of Nuclear and Particle Science*, 68, 237
 Fujimoto, M. Y., Ikeda, Y., & Iben, Icko, J. 2000, *ApJ*, 529, L25
 Gaia Collaboration, Katz, D., Antoja, T., et al. 2018, *A&A*, 616, A11
 Gehren, T., Liang, Y. C., Shi, J. R., Zhang, H. W., & Zhao, G. 2004, *A&A*, 413, 1045
 Goswami, A., Aoki, W., Beers, T. C., et al. 2006, *MNRAS*, 372, 343
 Goswami, A., Aoki, W., & Karinkuzhi, D. 2016, *MNRAS*, 455, 402
 Goswami, P. P., Rathour, R. S., & Goswami, A. 2021, *A&A*, 649, A49
 Hampel, M., Karakas, A. I., Stancliffe, R. J., Meyer, B. S., & Lugaro, M. 2019, *ApJ*, 887, 11
 Hampel, M., Stancliffe, R. J., Lugaro, M., & Meyer, B. S. 2016, *ApJ*, 831, 171
 Herwig, F. 2000, *A&A*, 360, 952
 Herwig, F., Langer, N., & Lugaro, M. 2003, *ApJ*, 593, 1056
 Herwig, F., Pignatari, M., Woodward, P. R., et al. 2011, *ApJ*, 727, 89
 Hidalgo, S. L., Pietrinferni, A., Cassisi, S., et al. 2018, *ApJ*, 856, 125
 Hill, V., Barbuy, B., Spite, M., et al. 2000, *A&A*, 353, 557
 Hollowell, D., Iben, Icko, J., & Fujimoto, M. Y. 1990, *ApJ*, 351, 245
 Iwamoto, N., Kajino, T., Mathews, G. J., Fujimoto, M. Y., & Aoki, W. 2004, *ApJ*, 602, 377
 Jones, S., Ritter, C., Herwig, F., et al. 2016, *MNRAS*, 455, 3848
 Jonsell, K., Barklem, P. S., Gustafsson, B., et al. 2006, *A&A*, 451, 651
 Karakas, A. I. & Lattanzio, J. C. 2014, *PASA*, 31, e030
 Lau, H. H. B., Stancliffe, R. J., & Tout, C. A. 2009, *MNRAS*, 396, 1046
 McWilliam, A. 1998, *AJ*, 115, 1640
 Noguchi, K., Aoki, W., Kawanomoto, S., et al. 2002, *PASJ*, 54, 855
 Piersanti, L., Cristallo, S., & Straniero, O. 2013, *ApJ*, 774, 98
 Qian, Y. Z. & Wasserburg, G. J. 2003, *ApJ*, 588, 1099
 Ramírez, I. & Meléndez, J. 2005, *ApJ*, 626, 465
 Schuler, S. C., Margheim, S. J., Sivarani, T., et al. 2008, *AJ*, 136, 2244
 Smith, V. V., Coleman, H., & Lambert, D. L. 1993, *ApJ*, 417, 287
 Sneden, C. A. 1973, PhD thesis, The University of Texas at Austin.
 Stancliffe, R. J., Dearborn, D. S. P., Lattanzio, J. C., Heap, S. A., & Campbell, S. W. 2011, *ApJ*, 742, 121
 Straniero, O., Gallino, R., & Cristallo, S. 2006, *Nucl. Phys. A*, 777, 311
 Yang, G.-C., Liang, Y.-C., Spite, M., et al. 2016, *Research in Astronomy and Astrophysics*, 16, 19
 Yong, D., Norris, J. E., Bessell, M. S., et al. 2013, *ApJ*, 762, 26

Appendix A: Line list

Table A.1. Equivalent widths (in mÅ) of lines used for the calculation of elemental abundances.

Wavelength (Å)	Element	E_{low} (eV)	log gf	HE 1005–1439
4132.06	Fe I	1.61	-0.650	77.1 (4.40)
4143.87		1.56	-0.450	77.7 (4.16)
4147.67		1.48	-2.104	28.5 (4.56)
4187.04		2.45	-0.548	49.0 (4.51)
4202.03		1.48	-0.708	91.1 (4.71)
4216.18		0.00	-3.356	35.9 (4.28)
4227.43		3.33	0.230	33.5 (4.34)
4233.60		2.48	-0.604	38.1 (4.35)
4250.12		2.47	-0.405	62.0 (4.67)
4250.79		1.56	-0.710	81.9 (4.49)
4260.47		2.40	-0.020	64.2 (4.26)
4375.93		0.00	-3.031	70.7 (4.66)
4383.55		1.48	0.200	127.1 (4.70)
4476.02		2.85	-0.570	30.1 (4.52)
4528.61		2.18	-0.822	62.0 (4.71)
4602.94		1.48	-1.950	37.3 (4.53)
4872.14		2.88	-0.600	25.7 (4.45)
4890.76		2.88	-0.430	39.2 (4.56)
4891.49		2.85	-0.140	51.8 (4.49)
4918.99		2.87	-0.370	35.6 (4.42)
4920.50		2.83	0.060	55.7 (4.36)
4994.13		0.92	-3.080	19.7 (4.58)
5006.12		2.83	-0.615	23.4 (4.34)
5171.60		1.49	-1.793	46.9 (4.50)
5192.34		3.00	-0.421	27.1 (4.41)
5194.94		1.56	-2.090	29.4 (4.53)
5216.27		1.61	-2.150	25.6 (4.56)
5226.86		3.04	-0.555	19.7 (4.39)
5227.19		1.56	-1.228	59.1 (4.24)
5232.94		2.94	-0.190	34.4 (4.27)
5266.56		3.00	-0.490	29.8 (4.54)
5269.54		0.86	-1.321	89.4 (4.16)
5270.36		1.61	-1.510	65.8 (4.71)
5324.18		3.21	-0.240	31.0 (4.54)
5328.04		0.91	-1.466	81.8 (4.18)
5328.53		1.56	-1.850	35.7 (4.41)
5446.92		0.99	-1.930	63.2 (4.34)
5455.61		1.01	-2.091	60.1 (4.46)
5497.52		1.01	-2.849	26.7 (4.58)
5506.78		0.99	-2.797	25.0 (4.46)
5586.76		3.37	-0.210	25.5 (4.54)
5615.64		3.33	-0.140	29.0 (4.50)
6136.61		2.45	-1.400	15.6 (4.41)
6230.72		2.56	-1.281	16.7 (4.44)
6494.98		2.40	-1.273	26.0 (4.48)
4491.40	Fe II	2.86	-2.700	7.6 (4.53)
4923.93		2.89	-1.320	51.3 (4.46)
5018.44		2.89	-1.220	56.5 (4.48)
5276.00		3.20	-1.940	16.2 (4.50)
5316.61		3.15	-1.850	20.9 (4.51)
5889.95	Na I	0.00	0.117	161.2 (4.56)
5895.92		0.00	-0.184	144.2 (4.60)
4571.10	Mg I	0.00	-5.691	16.0 (5.03)
5172.68		2.71	-0.402	125.9 (5.12)
5183.60		2.72	-0.180	138.4 (5.14)
5528.40		4.35	-0.620	33.4 (5.08)
4226.73	Ca I	0.00	0.243	144.6 (4.00)
4318.65		1.90	-0.208	22.1 (3.55)
4435.68		1.89	-0.500	26.9 (3.95)
4585.86		2.53	-0.186	10.4 (3.77)
5265.56		2.52	-0.260	13.4 (3.94)
5588.75		2.53	0.210	25.8 (3.84)
5594.46		2.52	-0.050	20.0 (3.93)
6122.22		1.89	-0.409	23.3 (3.68)
6162.17		1.90	0.100	36.4 (3.50)
6439.07		2.53	0.470	28.9 (3.63)
4246.82	Sc II	0.32	0.320	100.6 (0.89)
4415.56		0.60	-0.640	54.2 (0.75)
4981.73	Ti I	0.85	0.504	24.1 (2.31)
4991.06		0.84	0.380	12.6 (2.06)
5007.21		0.82	0.112	17.5 (2.48)
5210.39		0.05	-0.884	8.5 (2.24)

-continued

Wavelength (Å)	Element	E_{low} (eV)	log gf	HE 1005–1439
4290.22	Ti II	1.16	−1.120	63.8 (2.54)
4395.03		1.08	−0.660	75.7 (2.33)
4450.48		1.08	−1.450	28.5 (1.90)
4468.51		1.13	−0.600	72.3 (2.19)
4563.76		1.22	−0.960	63.3 (2.38)
4805.09		2.06	−1.100	16.6 (2.28)
5188.68		1.58	−1.210	31.0 (2.21)
5226.54		1.57	−1.300	20.2 (2.02)
4254.34	Cr I	0.00	−0.114	73.4 (2.60)
4274.80		0.00	−0.231	76.3 (2.80)
5204.51		0.94	−0.208	39.4 (2.66)
5206.04		0.94	0.019	39.9 (2.44)
5208.43		0.94	0.158	46.7 (2.46)
4030.75	Mn I	0.00	−0.470	81.7 (2.66)
4033.06		0.00	−0.618	72.1 (2.47)
4092.38	Co I	0.92	−0.940	14.9 (2.23)
4118.77		1.05	−0.490	25.9 (2.24)
4121.31		0.92	−0.320	33.3 (2.12)
5476.90	Ni I	1.83	−0.890	33.0 (3.40)
4077.71	Sr II	0.00	0.167	96.7 (−0.05)
4215.52		0.00	−0.145	98.9 (0.26)
4883.68	Y II	1.08	0.070	15.6 (−0.55)
4900.12		1.03	−0.090	12.5 (−0.57)
5087.42		1.08	−0.170	23.0 (−0.10)
5853.67	Ba II	0.60	−1.000	52.5 (0.37)
6141.71		0.70	−0.076	89.2 (0.65)
6496.90		0.60	−0.377	93.5 (0.90)
4086.71	La II	0.00	−0.150	31.6 (−0.69)
4123.22		0.32	0.120	29.4 (−0.66)
4921.78		0.24	−0.680	15.2 (−0.48)
4137.65	Ce II	0.52	0.246	14.3 (−0.26)
4486.91		0.30	−0.474	11.5 (0.05)
4562.36		0.48	0.081	20.5 (0.02)
4179.39	Pr II	0.20	0.310	15.7 (−0.76)
4061.08	Nd II	0.47	0.550	31.2 (−0.30)
4109.07		0.06	0.280	31.6 (−0.49)
4156.08		0.18	0.200	25.0 (−0.46)
4451.56		0.38	−0.040	20.5 (−0.17)
3944.68	Dy II	0.00	0.030	10.9 (−1.27)
4000.45		0.10	0.009	14.3 (−1.00)
4077.97		0.10	−0.058	6.4 (−1.36)
3896.23	Er II	0.05	−0.243	13.9 (−0.91)
3906.31		0.00	−0.052	13.0 (−1.20)
3793.38	Hf II	0.38	−0.950	6.7 (−0.72)
3918.09		0.45	−1.010	5.0 (−0.74)

The numbers in parentheses in column 5 give the derived abundances from the respective lines.